Chapter 6 (Part I)

An electrochemical study on lithium manganese oxide ($LiMn_2O_4$) for Al^{3+} ion storage in aqueous electrolyte

Nandi, S., and Das, S. K. *Phys. Chem. Chem. Phys.*, 23: 19150-19154, 2021

An electrochemical study on $LiMn_2O_4$ for Al^{3+} ion storage in aqueous electrolyte

6.1.1 Introduction

Chapters 2-5 discusses the electrochemistry of Al^{3+} ion insertion in graphite, bismuth-based compounds such as bismuth oxide (Bi_2O_3), bismuth oxychloride (BiOCl), vanadyl ethylene glycolate ($VO(CH_2O)_2$) and molydenium ditelluride ($MoTe_2$). In this chapter, the Al^{3+} ion storage in lithium manganese oxide ($LiMn_2O_4$) is discussed. $LiMn_2O_4$ is a cathode material of intense investigation for lithium-ion battery over several decades [1-6]. Keeping aside the excellent electrochemical properties, it attracted the interest again due to economic and safety factors [6]. Since $LiMn_2O_4$ could be considered to have attained a matured research stage, a vast pool of information is readily available for design of highly stable $LiMn_2O_4$ cathodes for facile Li^+ ion intercalation/deintercalation either in non-aqueous or aqueous electrolytes [7-10]. In fact, $LiMn_2O_4$ cathode was used for the first time in demonstrating the proof-of-concept of aqueous Li-ion battery [5]. However, the trivalent ion electrochemistry of $LiMn_2O_4$ is least explored with no piece of information available in the literature. A mere possibility of Al^{3+} ion insertion in $LiMn_2O_4$ bears significant impact in the further research of Al-metal or ion battery since it opens up a new avenue for exploring the well-established lithium-ion battery cathode materials for aluminum batteries. With this view in mind, the Al^{3+} ion insertion electrochemistry of $LiMn_2O_4$ in aqueous electrolyte is investigated in this chapter. It was revealed that Al^{3+} ion could indeed be inserted in $LiMn_2O_4$ initially via conversion and later on via intercalation processes.

6.1.2 Experimental Section

6.1.2.1 Materials

Lithium manganese oxide ($LiMn_2O_4$, Sigma Aldrich), Carbon black (Alfa Aesar), Ethanol and Distilled water.

6.1.2.2 Synthesis

Commercially available $LiMn_2O_4$ was used for this study. It was purchased from Sigma Aldrich (Product No. 482277) and no further treatment was performed prior to the study.

6.1.2.3 Characterization

The crystallographic phase identification was performed by using powder X-ray diffraction (XRD, BRUKER AXS D8 FOCUS; Cu-Kα radiation, λ = 1.5406 Å) with a scanning rate of 1^{o} min^{-1} in the 2θ range of 10-70^{o} at a generator voltage of 30 kV a current of 30 mA. The morphology was observed by field emission scanning electron microscopy (FESEM, JEOL JSM 7200F) and transmission electron microscopy (TEM, FEI TecnaiG2 20 S-TWIN) at an accelerating voltage of 200 kV. XPS was recorded with Thermo-Scientific ESCALAB Xi^{+} spectrometer with a monochromatic Al Kα X-ray source (1486.6 eV).

6.1.2.4 Electrochemical analysis

Electrode slurry was prepared by mixing $LiMn_2O_4$ powder with carbon black (Alfa Aesar Product No. H30253) and polyvinylidene fluoride (PVDF) with weight proportion of 70:20:10 in N-methyl-2-pyrrolidone (NMP). This prepared slurry was coated on titanium substrate (breadth 1 cm and length 1.5 cm) and dried at 120 ^{o}C for 12 h. The mass loading of the material was approximately 2.5-3.5 mg.

Cyclic voltammetry (CV) and galvanostatic discharge/charge experiments were performed in a glass cell (diameter 2.7cm, height 2.2 cm) using Biologic SP300 electrochemical work station. Pt electrode and aqueous Ag/AgCl electrode were used as the counter and reference electrodes respectively for three electrode system measurements. The utilized electrolytes were 1 M LiCl and 1 M $AlCl_3$ aqueous electrolytes unless otherwise stated. All the electrochemical experiments were conducted at room temperature (25 ^{o}C). For ex-situ XRD, SEM and XPS measurements, the electrodes were harvested after required discharge/charge cycles and washed with deionized water and dried at 110 ^{o}C for 24 hr. For ex-situ XRD, electrodes were prepared with graphite current collector. All the electrochemical experiments were conducted at room temperature (25 ^{o}C).

6.1.3 Results and Discussion

Commercially available $LiMn_2O_4$ was used for this study without any further processing. The XRD pattern shown in Figure 6.1.1a confirms the crystalline phase of $LiMn_2O_4$ (JCPDS-35-0782, space group $Fd\bar{3}m$). FESEM (Figure

6.1.1b) and TEM (Figure 6.1.1c) images indicate existence of micrometer sized $LiMn_2O_4$ particles.

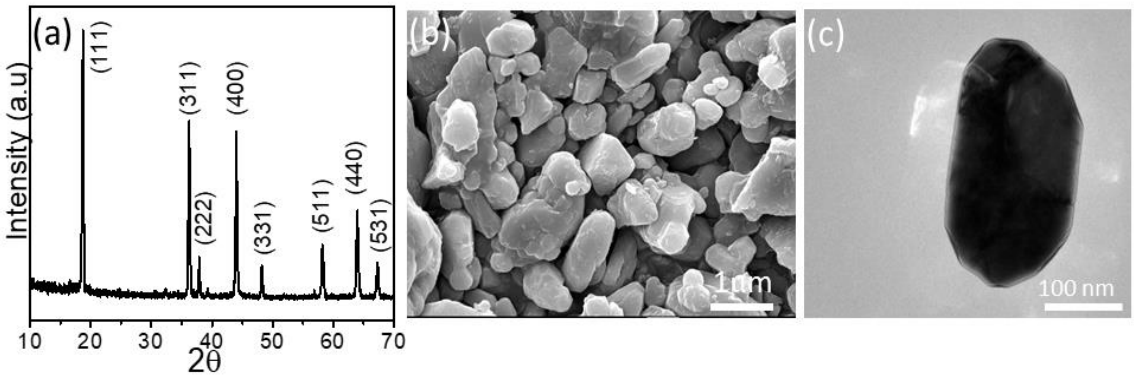

Figure 6.1.1 XRD pattern, (b) FESEM image and (c) TEM image of $LiMn_2O_4$.

First, in order to verify whether Li^+ ion from aqueous electrolyte could be intercalated in the $LiMn_2O_4$ phase or not, CV experiment was performed in 1 M LiCl aqueous electrolyte in a voltage range of -0.1 V to 1.5 V. Redox activities could be observed as shown in Figure 6.1.2a. A prominent cathodic peak (A) at 0.35 V (vs Ag/AgCl) and two anodic peaks (B) at 1.0 V and (C) 1.21 V (vs Ag/AgCl) could be easily seen. A minor cathodic hump at 0.6 V (peak at D) is also present. It is fairly in corroboration with the previous reports on $LiMn_2O_4$ in aqueous system [10]. Relying on it, the Al^{3+} ion electrochemistry of $LiMn_2O_4$ is investigated in aqueous system. Figure 6.1.2b shows the CV profiles of $LiMn_2O_4$ in 1 M $AlCl_3$ aqueous electrolyte in a voltage range of 0.2 V to 2 V from 2nd cycle onward. There exists a highly reversible pair of very prominent cathodic and anodic peaks respectively at 1.54 V (peak A$^{/}$) and 1.88 V (peak B$^{/}$) in addition to a small cathodic peak at 1.85 V (peak C$^{/}$). The cathodic peaks may be assigned due to intercalation of Al^{3+} ion in $LiMn_2O_4$, while the anodic peak can be correspond due to de-intercalation of Al^{3+} ion in $LiMn_2O_4$. The potential is measured w.r.t. Al. However, the 1st cathodic cycle (Figure 6.1.3a) unusually shows a broad peak centered at 1 V, which is completely different from the rest of the cycles. Contrary to $AlCl_3$ aqueous electrolyte, the CV profiles obtained with 0.5 M $Al_2(SO_4)_3$ and 1 M $Al(NO_3)_3$ aqueous electrolytes are completely different. As shown in Figure 6.1.2c, only one cathodic peak at 1 V (peak E) could be seen and there is no signature of any reversible anodic peak in the case of $Al_2(SO_4)_3$ aqueous electrolytes. Moreover, the 1st cycle also does not show any similar characteristics as was seen in $AlCl_3$ electrolyte. Interestingly, no electrochemical activity could be seen at all in the case of $Al(NO_3)_3$ electrolytes (Figure 6.1.3b) in any

of the scans. Experiments were also performed in 0.5 M H_2SO_4 solution to identify any possibility of reversible proton intercalation in $LiMn_2O_4$. However, CV profiles (Figure 6.1.3c) indicate only a broad low intensity hump centered at 1.6 V in the cathodic cycles with no indication of any reversibility in the anodic cycles. Hence, there may be a possibility of small amount of irreversible proton intercalation in $LiMn_2O_4$. To identify the Al^{3+} ion insertion process is an intercalation or not, CV experiments were performed at different scan rates in $AlCl_3$ electrolytes (Figure 6.1.4). Clearly, as shown in Figure 6.1.2d, both the cathodic and anodic peak current responses (I) exhibit a linear dependence with scan rates (γ) according to the equation $I=k\gamma^{0.5}$ (k is a constant). This further signifies a diffusion-controlled Al^{3+} ion intercalation and de-intercalation processes in $LiMn_2O_4$ [11].

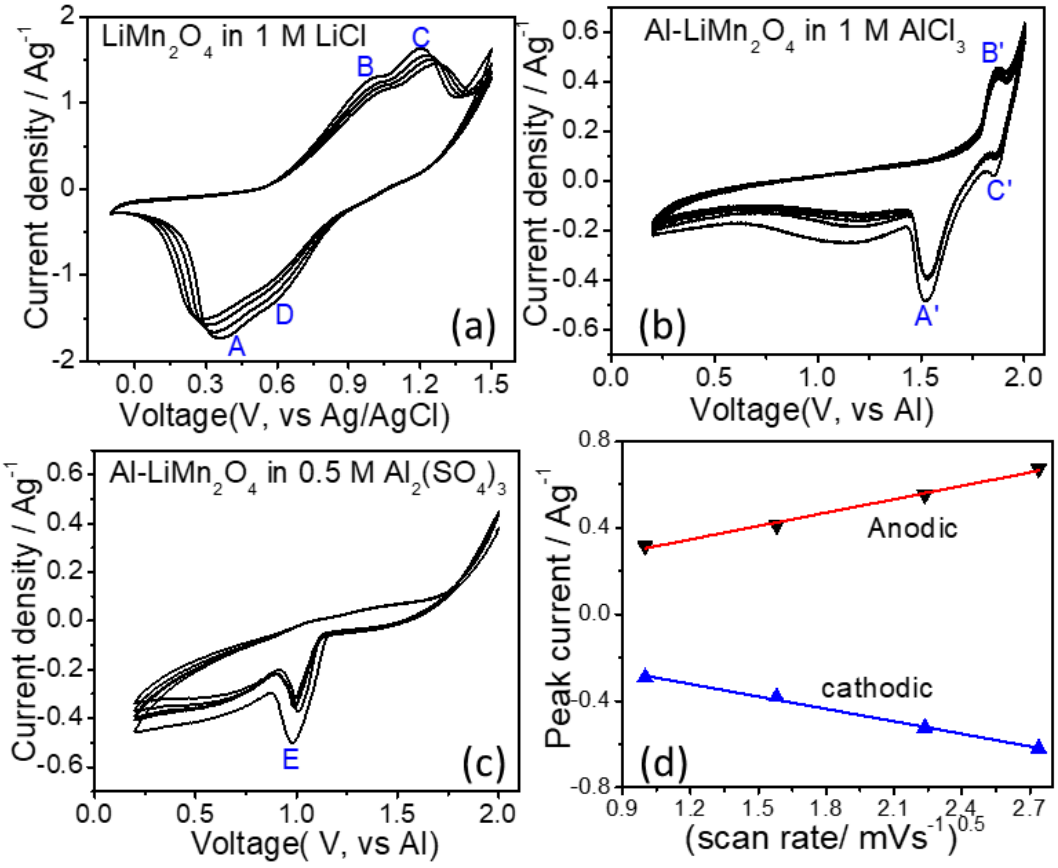

Figure 6.1.2 CV curves of $LiMn_2O_4$ in (a) 1 M LiCl, (b) 1 M $AlCl_3$, (c) 0.5 M $Al_2(SO_4)_3$ aqueous electrolytes at scan rate of 2.5 mVs^{-1} and (d) variation of redox peak current versus scan rate according to equation $I=k\gamma^{0.5}$ (k is a constant).

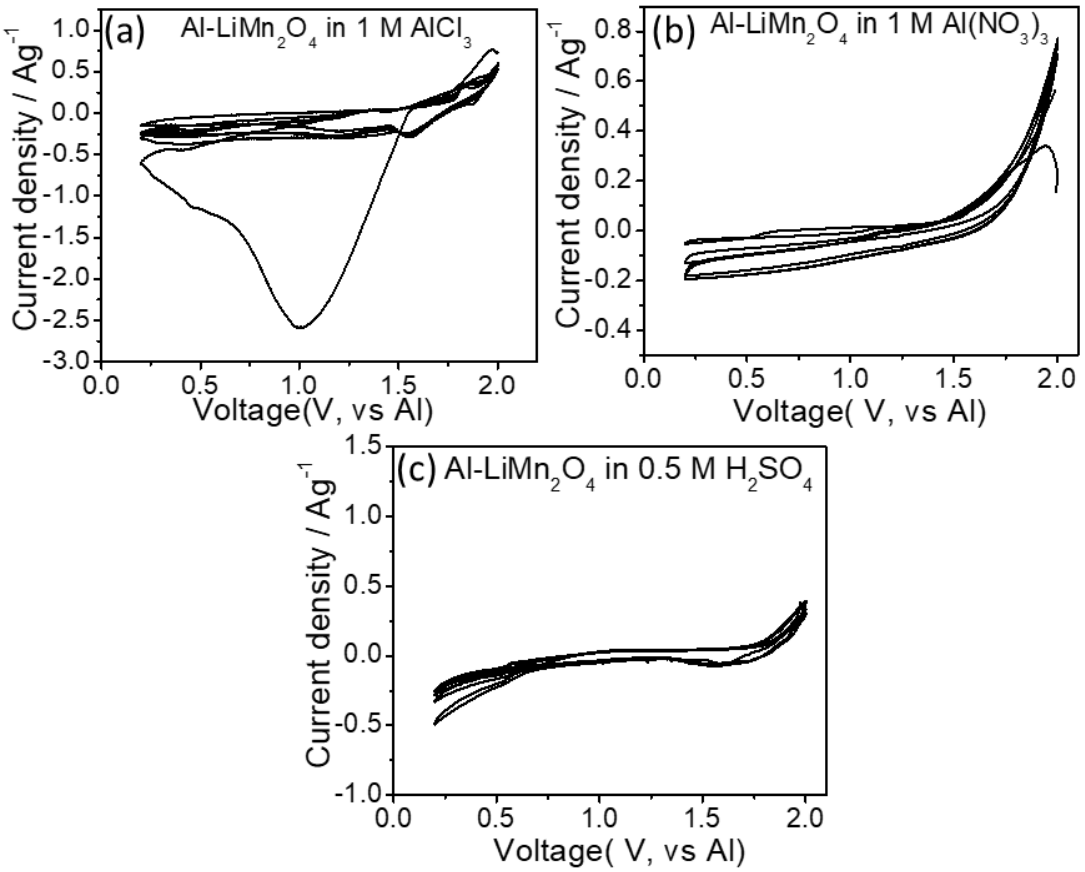

Figure 6.1.3 CV curves of $LiMn_2O_4$ in (a) 1 M $AlCl_3$, (b) 1 M $Al(NO_3)_3$, and (c) 0.5 M H_2SO_4 aqueous electrolyte at a scan rate of 2.5 mVs^{-1}.

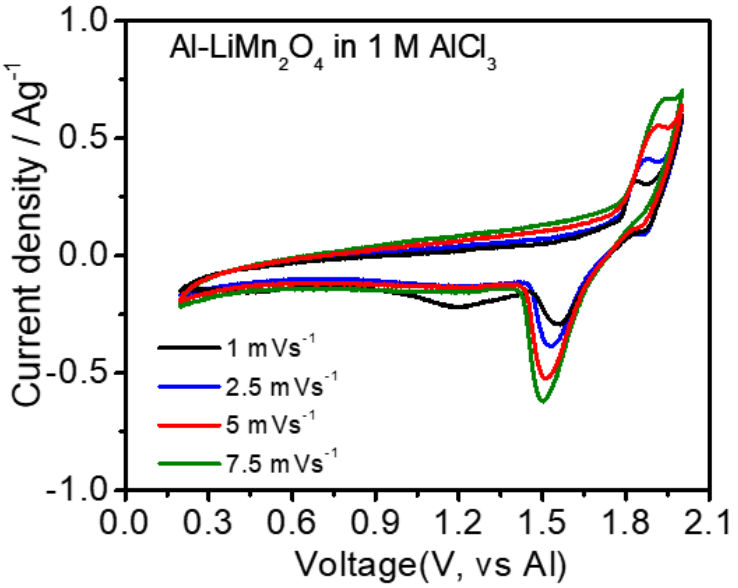

Figure 6.1.4 CV curves of $LiMn_2O_4$ in 1 M $AlCl_3$ aqueous electrolyte at different scan rates.

Galvanostatic discharge/charge experiments were performed to estimate the Al^{3+} ion storage capacities of $LiMn_2O_4$ in a voltage range of 0.2 V to 2 V. Figure 6.1.5a shows the discharge/charge profiles (after 1st discharge cycle) of $LiMn_2O_4$ in 1 M $AlCl_3$ aqueous electrolyte at a specific current of 200 mAg^{-1}. The cell shows very high degree of reversibility. The discharge and charge profiles show distinct potential plateaus at 1.5 V and 1.85 V (vs Al) respectively. This is absolutely in agreement with the CV profiles (Figure 6.1.2b). The second discharge and charge capacities are 140 $mAhg^{-1}$ and 110 $mAhg^{-1}$ respectively. There is a gradual decline in capacity and the discharge capacity is 40 $mAhg^{-1}$ at the 15th cycle (Figure 6.1.5b). Similarly, the cell was tested at a high specific current rate of 600 mAg^{-1}. As shown in Figure 6.1.5c, the potential plateaus could be seen. At the end of 120 cycles, the discharge capacity is found to be approximately 20 $mAhg^{-1}$ (Figure 6.1.5d). It is interesting to note that the initial (1st cycle) discharge capacity is exceptionally high in all investigate cases as shown in Figure 6.1.6. It is found to be 1125 $mAhg^{-1}$ and 641 $mAhg^{-1}$ at current rates of 200 mAg^{-1} and 600 mAg^{-1} respectively. In addition, the initial discharge profile is significantly different than the rest of the discharge cycles, which is consistent with the CV profiles (Figure 6.1.3a). On the other hand, $LiMn_2O_4$ could not be cycled at any current rates with $Al_2(SO_4)_3$ and $Al(NO_3)_3$ aqueous electrolytes (Figure 6.1.7a and 6.1.7b). Capacity fading in pristine $LiMn_2O_4$ is a well-known phenomenon which is mostly ascribed to the dissolution of Mn species in acidic environment [6]. In an effort to mitigate this issue, a finite amount of low-valence Mn salt was introduced in the system [12-13]. It was found that addition of 0.25 M $MnCl_2$ in the 1 M $AlCl_3$ aqueous electrolyte could not only significantly improve the Al^{3+} ion storage capacities of $LiMn_2O_4$ but also provides better cycling stability (Figure 6.1.5e, f). At a current rate of 800 mAg^{-1}, a discharge capacity of 65 $mAhg^{-1}$ is achieved at the 75th cycle. The discharge and charge potential plateaus are still maintained at the same potentials as observed for pristine $AlCl_3$ aqueous electrolyte. Another striking and important feature of $LiMn_2O_4$ is that it exhibits exceptionally negligible self-discharge. Figure 6.1.8 shows the variation of the open circuit potential of an Al-$LiMn_2O_4$ cell with time. It was measured after charging the cell up to 2 V. It is observed that the

cell maintains a very steady potential of 1.5 V for 24 h signifying the high stability of the cell.

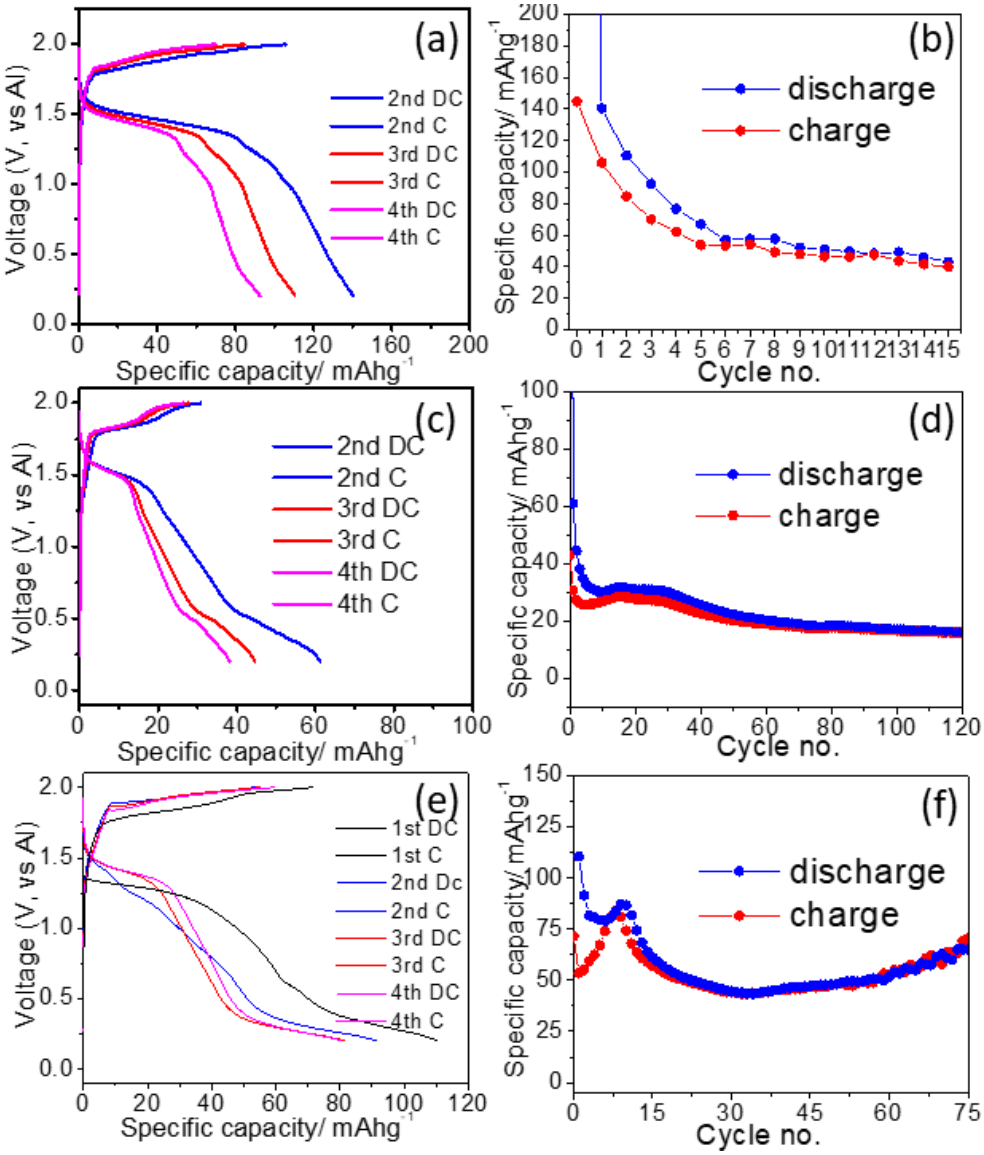

Figure 6.1.5 Galvanostatic discharge/charge curves and variation of specific capacities of $LiMn_2O_4$ in 1 M $AlCl_3$ electrolyte at a current rate of (a, b) 200 mAg^{-1}, (c, d) 600 mAg^{-1} and (e, f) in a mixture of 1 M $AlCl_3$ and 0.25 M $MnCl_2$ aqueous electrolyte at current of 800 mAg^{-1}. DC: discharge cycle, C-charge cycle.

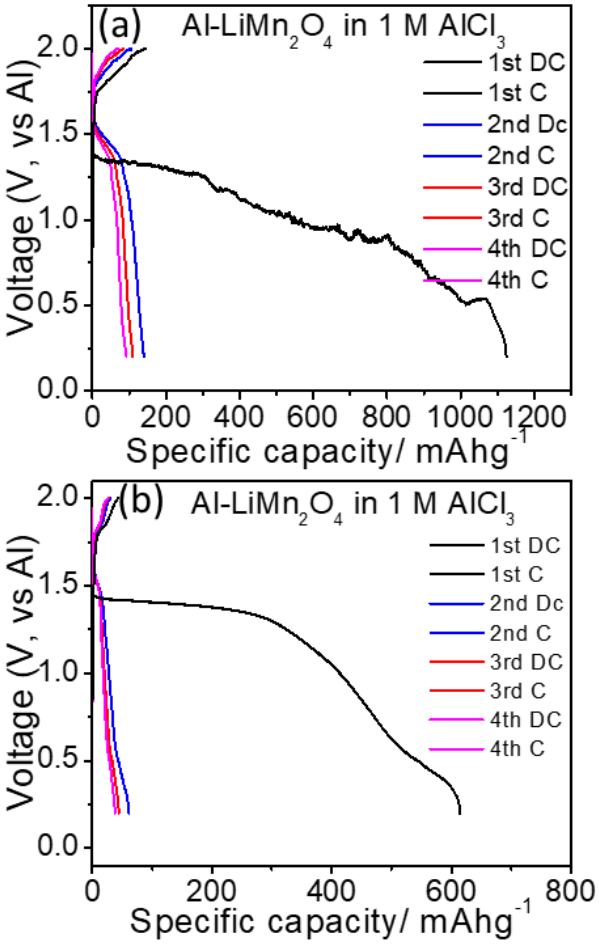

Figure 6.1.6 Galvanostatic discharge/charge curves of $LiMn_2O_4$ in 1 M $AlCl_3$ at a current rate of (a) 200 mAg^{-1} and (b) 600 mAg^{-1}. DC-discharge cycle, C-charge cycle.

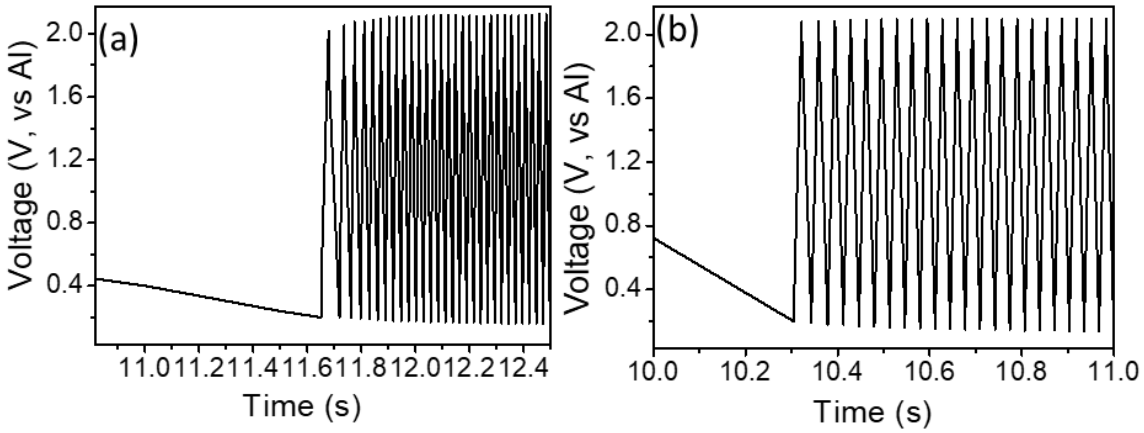

Figure 6.1.7 Galvanostatic discharge/charge curves of $LiMn_2O_4$ in (a) 0.5 M $Al_2(SO_4)_3$, and (b) 1 M $Al(NO_3)_3$ aqueous electrolytes. The current rate is 200 mAg^{-1}.

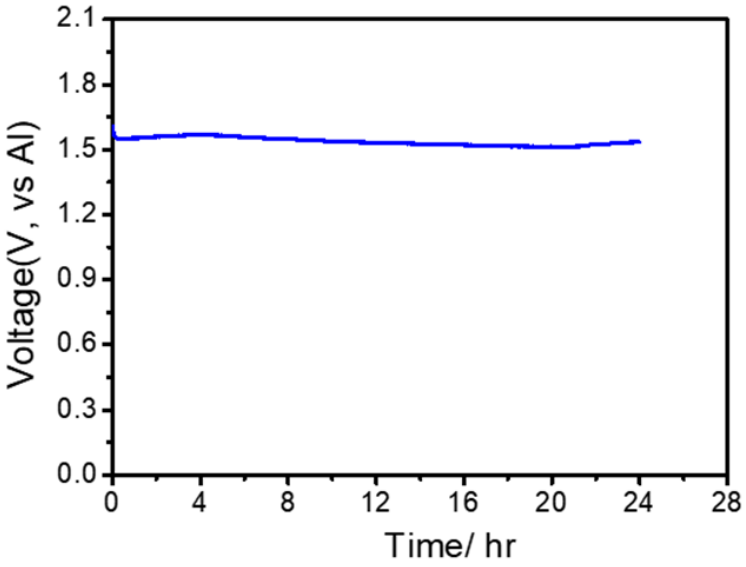

Figure 6.1.8 Self-discharge profile of Al-$LiMn_2O_4$ cell in 1 M $AlCl_3$ aqueous electrolyte.

To shed light on the electrochemical mechanism undergoing on the $LiMn_2O_4$ cathode, the charged-discharged state electrodes were analyzed with ex-situ microscopy and spectroscopy techniques. Ex-situ FESEM images (Figure 6.1.9b and 6.1.10b) of the 1st discharge state electrode show complete disintegration of the micrometer sized $LiMn_2O_4$ particles. Besides, there is an appearance of a smooth and compact polymer type layer (Figure 6.1.10b). The charging however results in disappearance of this layer (Figure 6.1.9c) and few nanosized particles alongside carbon black could be observed (Figure 6.1.10c). In consistent with the ex-situ FESEM images, as shown in Figure 6.1.9d, ex-situ XRD pattern of 1st discharged state electrode also shows complete loss of $LiMn_2O_4$ crystal phase. Rather, few new diffraction peaks appeared after 1st charge. These are observed at $2\theta = 22.5^o$, 37^o and 65.6^o which correspond to γ-MnO_2 (JCPDS no. 44-0644). The other peak at $2\theta = 18.9^o$ belongs to $LiMn_2O_4$. This peak may appear due to some unreacted residual $LiMn_2O_4$ particle in the electrode. FESEM images also show existence of such particles after 1st charge (Figure 6.1.9c). There is also a new diffraction peak $2\theta = 44.45^o$ which corresponds to pure phase of Al (JCPDS no. 004-0787). This diffraction peak is also observed after 2nd discharge. Besides this, ex-situ XPS measurement was also carried out. As show in Figure 6.1.9e, Al 2*p* peak at 74.9 eV could be observed for both the 1st discharged and 1st charged state electrodes signifying

presence of Al [13-14]. Elemental mapping and energy dispersive X-ray spectra (EDX) also show presence of Al in both these electrodes (Figure 6.1.11 and Figure 6.1.12). Similarly, the Mn 2*p* peak (Figure 6.1.9f) is composed of two doublets with binding energies located at 642.5 eV and 654.4 eV, corresponding to Mn $2p_{3/2}$ and Mn $2p_{1/2}$, which fall in the respective ranges of Mn^{3+} and Mn^{4+} oxidation states respectively [15]. However, both these peaks are slightly shifted to lower binding energies, which may be attributed to reduction of $LiMn_2O_4$ after the 1st discharge. There is also a change in the Li 1s spectrum. As shown in Figure 6.1.13a, there is almost no trace of Li 1*s* peak, which is located at 54.2 eV, after the 1st discharge/charge signifying a possible structural transformation of $LiMn_2O_4$ during the intercalation/deintercalation process of Al^{3+} ions. Furthermore, as shown in Figure 6.1.13b, the peaks at 530.2 eV and 531.5 eV which could be seen for the pristine $LiMn_2O_4$ electrode represent Mn-O-Mn and Mn-OH bonds [15]. However, the minor peak at 531.5 eV is shifted to higher binding energy (532.39 eV) after the 1st discharge/charge state, which approximately falls in the binding energy range of Al-O-OH [16]. Based on the above-mentioned analysis, the following could be inferred. First, the $LiMn_2O_4$ losses its crystal structure upon Al^{3+} ion intercalation during the first discharge and possibly produces an amorphous phase of MnO_2. The $LiMn_2O_4$ does not regain its original structure upon subsequent charging. Second, the presence of Al in the ex-situ XRD patterns also hints at possible formation of Al-Li alloy. The exact phase is unknown though. Third, the amorphous MnO_2 phase turns to nanocrystalline MnO_2 phase upon Al^{3+} ion deintercalation and this process of phase transformation continues in subsequent cycles. Therefore, the following possible reaction mechanism could be proposed: during first discharge (i) $2LiMn_2O_4 + 3xAl^{3+} + 9xe^- \xrightarrow{\text{1st discharge}} 3Al_xMnO_2\text{(amorphous)} + Li_2O + MnO$ and during subsequent charge-discharge cycles (ii) Al_xMnO_2 (amorphous) $\underset{\text{discharge}}{\overset{\text{charge}}{\rightleftharpoons}}$ MnO_2 (crystalline) + xAl^{3+} + $3xe^-$.

The Li_2O and MnO produced during the 1st discharge may dissolve in the acidic $AlCl_3$ aqueous electrolyte (pH ~ 3) [17].

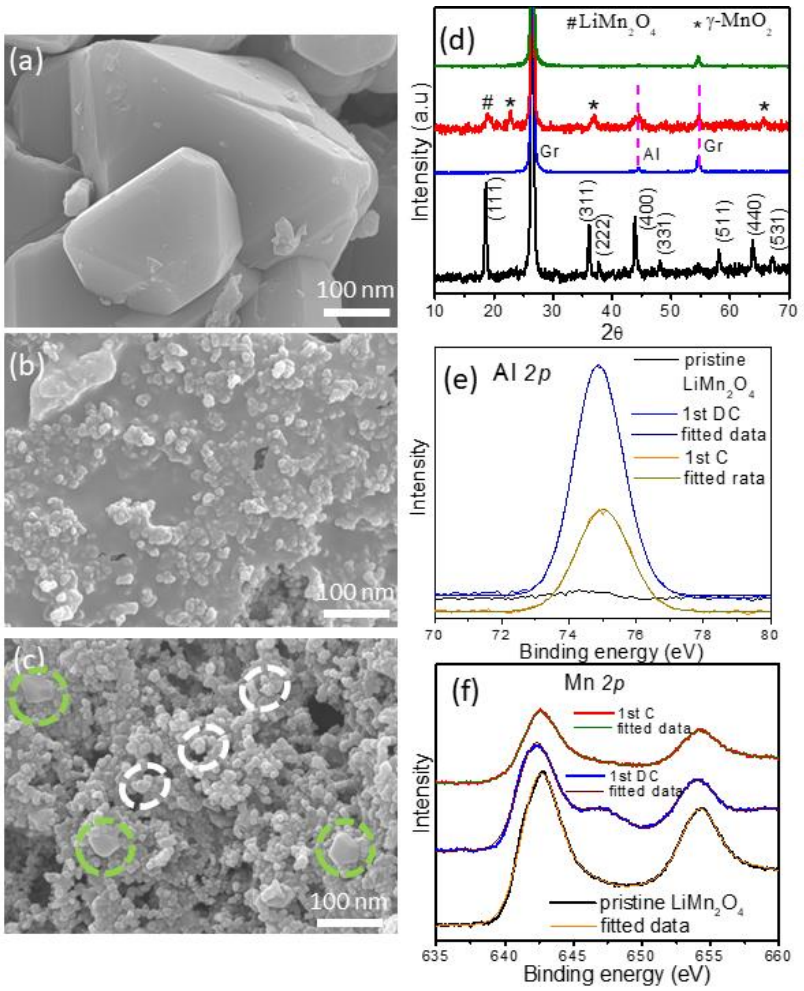

Figure 6.1.9 FESEM images of (a) pristine $LiMn_2O_4$, (b) after 1st discharge and (c) 1st charge $LiMn_2O_4$ electrodes. (d) Ex-situ XRD patterns (black-pristine $LiMn_2O_4$, blue-after 1st discharge, red-after 1st charge, green-after 2nd discharge), Ex-situ XPS spectra of (e) Al 2*p* and (f) Mn 2*p* of pristine $LiMn_2O_4$, after 1st discharge and after 1st charge. White circles and green circles in Figure 6.1.9c respectively represent carbon black and residual $LiMn_2O_4$ particles. Gr-graphite peaks. Ex-situ XRD was performed using graphite current collector.

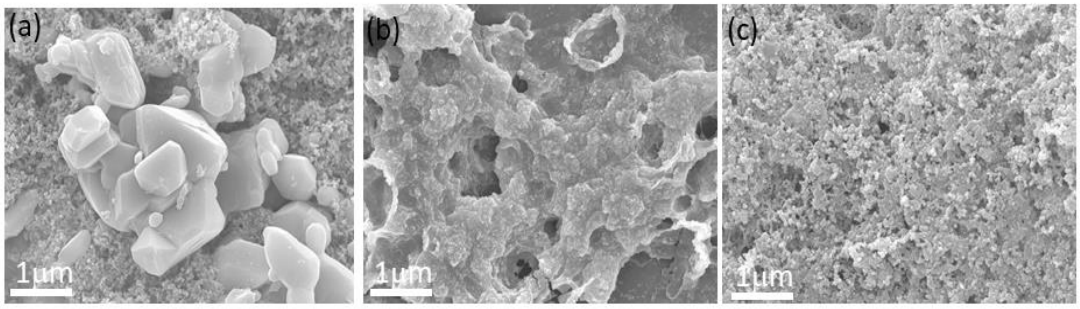

Figure 6.1.10 Ex-situ FESEM images of $LiMn_2O_4$ electrode (a) before discharge, (b) after 1st discharge and (c) after 1st charge. Scale bar = 1 µm.

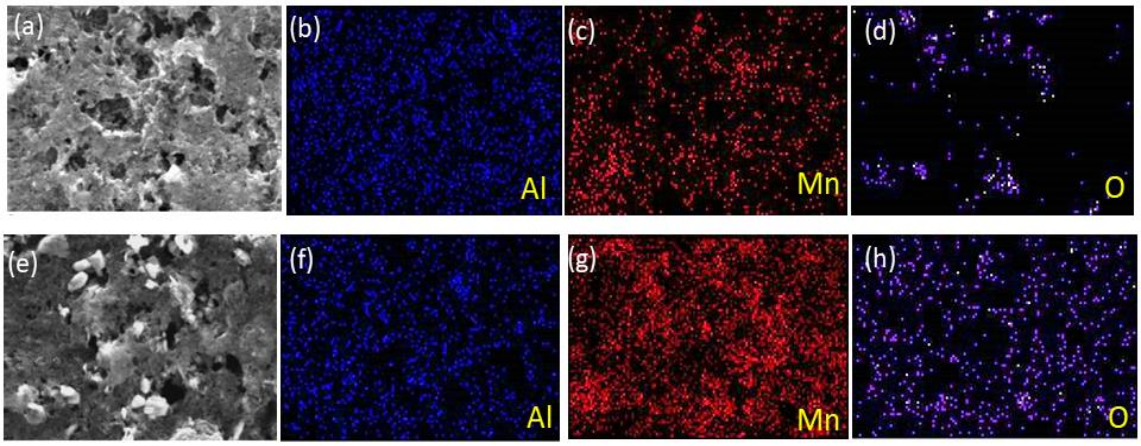

Figure 6.1.11 (a) SEM image of scanned area for elemental mapping of 1st discharge state $LiMn_2O_4$ electrode. Elemental mapping images of (b) Al, (c) Mn and (d) O of the 1st discharge state electrode. (e) SEM image of scanned area for elemental mapping of 1st charge state $LiMn_2O_4$ electrode. Elemental mapping images of (f) Al, (g) Mn and (h) O of the 1st charge state electrode.

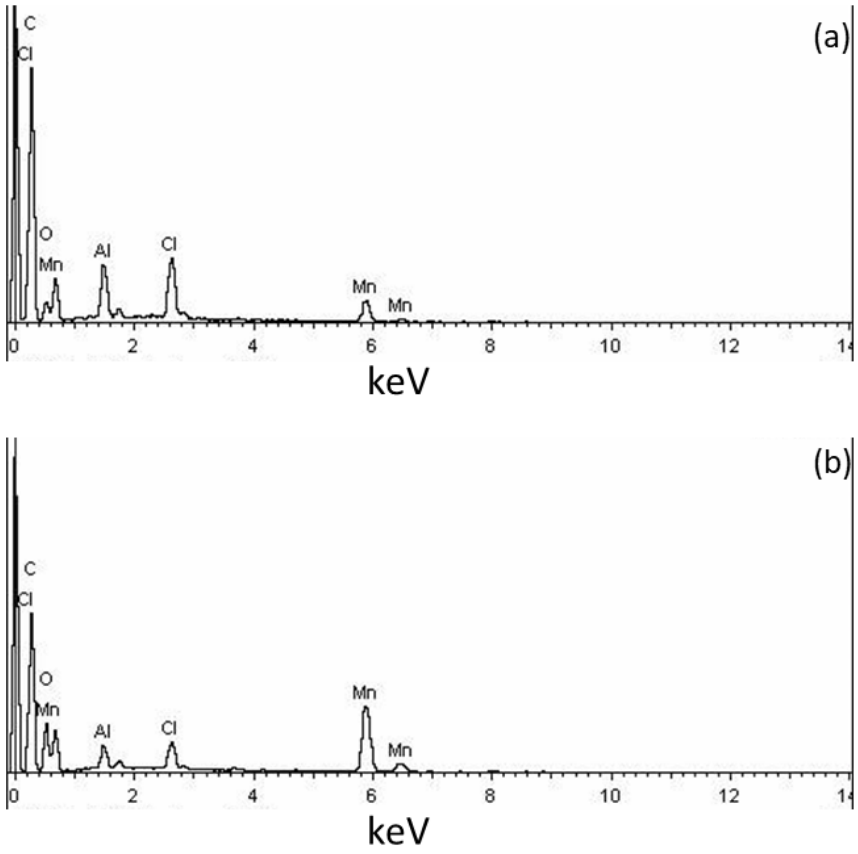

Figure 6.1.12 Energy dispersive X-ray (EDX) spectrum of $LiMn_2O_4$ (a) after 1st discharge state electrode and (b) after 1st charge electrode.

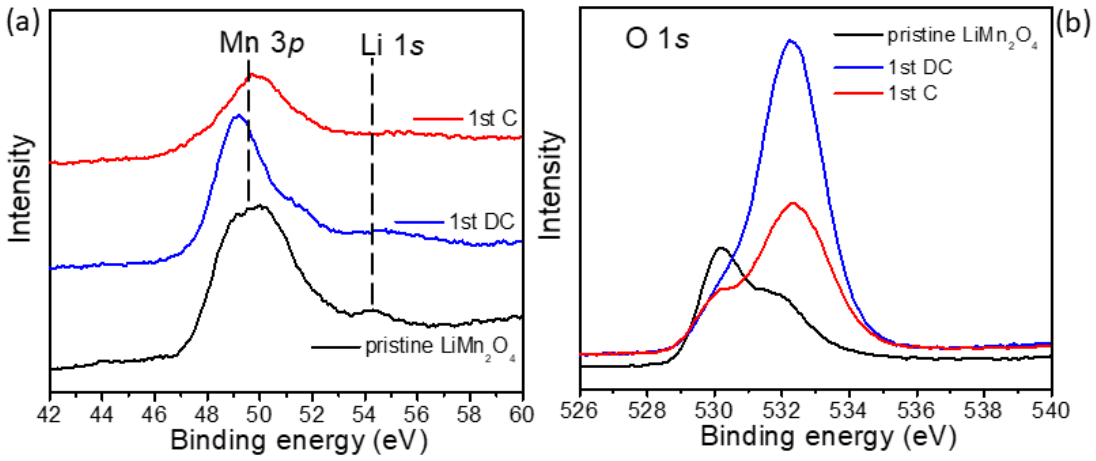

Figure 6.1.13 (a) Li 1*s* and (b) O 1*s* XPS spectra of $LiMn_2O_4$ electrode before discharge, after 1st discharge and after 1st charge.

6.1.4 Conclusion

In summary, the possibility of Al^{3+} ion intercalation/extraction in $LiMn_2O_4$ in aqueous medium is demonstrated. It is noticed that Al^{3+} ion intercalation process completely destroys the crystal structure of $LiMn_2O_4$ after first discharge with concomitant rise of a new phase of MnO_2. Moreover, when tested with reference to an Al anode, $LiMn_2O_4$ shows an almost flat discharge plateau at 1.5 V with a very low polarization (< 0.4 V). Interestingly, the discharge capacity could be significantly enhanced by pre-addition of a low-valence Mn salt in the electrolyte and it is seen that a discharge capacity of 65 $mAhg^{-1}$ could be achieved at a higher current rate of 800 mAg^{-1} at the 75^{th} cycle. Moreover, the Al-$LiMn_2O_4$ cell demonstrates remarkably low self-discharge.

6.1.5 References

[1] Thackeray, M., Johnson, P., Picciotto, L. de, Bruce, P., and Goodenough, J.B. Electrochemical extraction of lithium from $LiMn_2O_4$. *Mater.Res.Bull.*, 19:179, 1984.

[2] Thackeray, M., Picciotto, L. de, Kock, A. de, Johnson, P., Nicholas, V., and Dendorff, K. Spinel electrodes for lithium batteries — A review. *J. Power Sources*, 21: 1, 1987.

[3] Li, W., Dahn, J. R., and Wainwright, D. S. Rechargeable lithium batteries with aqueous electrolytes. *Sci.*, 264: 1115, 1994.

[4] Whittingham, M. S. Lithium batteries and cathode materials. *Chem. Rev.*, 104: 4271, 2004.

[5] Li, W., and Dahn, J. R. Lithium-ion cells with aqueous electrolytes. *J. Electrochem. Soc*., 142: 1742, 1995.

[6] Manthiram, A. A reflection on lithium-ion battery cathode chemistry *Nat. Commun.*, 11: 1550, 2020.

[7] Li, N. C., Patrissi, C. J., Che, G. L., and Martin, C. R., Rate capabilities of nanostructured $LiMn_2O_4$ electrodes in aqueous electrolyte. *J. Electrochem. Soc.,* 147: 2044, 2000.

[8] Tian, L., and Yuan, A. B. Electrochemical performance of nanostructured spinel $LiMn_2O_4$ in different aqueous electrolytes. *J. Power Sources*, 192: 693, 2009.

[9] Jiang, H., Fu, Y., Hu, Y., Yan, C., Zhang, L., Lee, P.S., and Li, C. Hollow $LiMn_2O_4$ nanocones as superior cathode materials for lithium-ion batteries with enhanced power and cycle performances. *Small*, 10:1096-1100, 2014.

[10] Liu, S., Ye, S. H., Li, C. Z., Pan, G. L., and Gao, X. P. Rechargeable aqueous lithium-ion battery of TiO_2/$LiMn_2O_4$ with a high voltage. *J. Electrochem. Soc.* 158: A1490-A1497, 2011.

[11] Wang, J., Polleux, J., Lim, J., and Dunn, B. Pseudocapacitive contributions to electrochemical energy storage in TiO_2 (anatase) nanoparticles. *J. Phys. Chem. C.*, 111:14925-14931, 2007.

[12] Zhao, Q., Zachman, M. J., Sadat, W. I. Al., Zheng, J., Kourkoutis, L. F., and Archer, L. Solid electrolyte interphases for high-energy aqueous aluminum electrochemical cells. *Sci. Adv.*, 4:8131, 2018.

[13] Zhang, N., Cheng, F., Liu, J., Wang, L., Long, X., Liu, X., Li, F., and Chen, J. Rechargeable aqueous zinc-manganese dioxide batteries with high energy and power densities. *Nat. Commun.*, 8: 405, 2017.

[14] Lin, M. C., Gong, M., Lu, B., Wu, Y., Wang, D. Y., Guan, M., Angell, M., Chen, C., Yang, J., Hwang, B. J., and Dai, H. An ultrafast rechargeable aluminum-ion battery. *Nat.*, 520(7547):324, 2015.

[15] Wang, J., Wang, J. G., Liu, H., Wei, C., and Kang, F. Zinc ion stabilized MnO_2 nanospheres for high capacity and long lifespan aqueous zinc-ion batteries. *J. Mater. Chem. A*, 7: 13727–13735, 2019.

[16] Yang, Y., Cheng, J., Liu, S., Wang, H., and Dong, P. Effect of $NaAlO_2$ sealing on corrosion resistance of 2024 aluminum alloy anodized film. *Mater. Corros.*, 70: 120–127, 2019.

[17] Jang, D. H., and Oh, S. M. Electrolyte effects on spinel dissolution and cathodic capacity losses in 4 V $Li/Li_xMn_2O_4$ rechargeable cells. *J. Electrochem. Soc.*, 144:3342–3348, 1997.

Chapter 6 (Part II)

Reversible Al^{3+} ion storage in lithium manganese phosphate ($LiMnPO_4$) for aqueous electrolyte

Nandi, S., and Das, S. K. Nandi, S., and Das, S. K. (*Under review*, 2022).

Reversible Al^{3+} ion storage in lithium manganese phosphate ($LiMnPO_4$) in aqueous electrolyte

6.2.1 Introduction

In the previous chapter, the electrochemistry of Al^{3+} ion insertion in lithium manganese phosphate ($LiMn_2O_4$) was discussed. It was found that $LiMn_2O_4$ can indeed store Al^{3+} ion and it shows a flat discharge plateau at 1.5 V (vs Al) with a very low polarization (~ 0.4 V). Therefore, with this view in mind, this chapter explores the electrochemical possibility of Al^{3+} ion insertion in lithium manganese phosphate ($LiMnPO_4$) in aqueous electrolyte. $LiMnPO_4$ is a well-known cathode material for non-aqueous lithium-ion battery with theoretical capacity of 170 $mAhg^{-1}$. This material is promising because of low toxicity, safety, easy processing and rich electrochemical properties [1-4]. The Al^{3+} ion electrochemistry of $LiMnPO_4$ in either aqueous or non-aqueous electrolyte is hitherto been unknown. Therefore, the electrochemical behavior of $LiMnPO_4$ in an Al^{3+} ion cell is investigated and found that $LiMnPO_4$ exhibits distinct discharge and charge potential plateaus with reasonably high storage specific capacity.

6.2.2 Experimental Section

6.2.2.1 Materials

Sodium sulfide nonahydrate ($Na_2S{\cdot}9H_2O$, Sigma Aldrich), Lithium sulfate monohydrate ($Li_2SO_4{\cdot}H_2O$, Sigma Aldrich), Manganese sulfate monohydrate ($MnSO_4{\cdot}H_2O$, Sigma Aldrich), Ethanol and Distilled water.

6.2.2.2 Synthesis

$LiMnPO_4$ was synthesized by a hydrothermal method as reported in ref [5]. Briefly to describe, an aqueous mixture of 14 mmol of $Na_2S{\cdot}9H_2O$, 40 mmol $Li_2SO_4{\cdot}H_2O$, 20 mmol $MnSO_4{\cdot}H_2O$ and 20 mmol of $NH_4H_2PO_4$ was heated at 200 ^oC for 10 h in a Teflon-lined stainless-steel autoclave. Afterwards, the solution was cooled down to room temperature and the resulted white precipitate was collected by centrifugation followed by washing with deionized water and ethanol and finally the product was dried at 60 ^oC for 12 h.

WO_3 was synthesized by a hydrothermal method [8]. Briefly, 0.825 g of Na_2WO_4 .$2H_2O$ and 0.290 g of NaCl were dissolved in 19 ml of deionized water and the pH was adjusted to 2 by 3 M HCl. The resulting solution was heated at 180 ^oC for 24 h in an autoclave. The resultant precipitate was collected after cooling and washed with deionized water and ethanol followed by drying at 80 ^oC for 12 h.

6.2.2.3 Characterization

The material was characterized by powder X-ray diffraction (BRUKER AXS D8 FOCUS; Cu-K_α radiation, λ = 1.5406 Å) and the morphologies of the samples were characterized using field emission electron microscopy (FESEM, ZEISS Supra 40V) and transmission electron microscopy (TEM, JEOL-2010 F).

6.2.2.4 Electrochemical analysis

Electrode slurries were prepared separately for $LiMnPO_4$ cathode and WO_3 anode using Super P, polyvinylidene fluoride with a weight ratio of 70:20:10 in N-methyl-2-pyrrolidone as solvent. The slurry was drop cast on pristine carbon cloth (Panex PWO6 carbon fiber, Product code: 625304, USA) and dried at 90 ^oC for 12 h. Cyclic voltammetry (CV) and galvanostatic discharge/charge experiments were conducted in a conventional three-electrode electrochemical glass cell in a voltage range of -0.3 V to 1.2 V (vs Ag/AgCl), where $LiMnPO_4$ act as the working electrode, Pt and Ag/AgCl were used as the counter and reference electrodes respectively. The used electrolytes were 1 M LiCl and 1 M $AlCl_3$ aqueous electrolyte. All the electrochemical experiments were conducted at room temperature (25 ^oC).

An aqueous Al-ion full cell was tested with WO_3 as anode and $LiMnPO_4$ as cathode. The utilized electrolyte was 1 M $AlCl_3$ aqueous solution. The galvanostatic discharge/charge and CV experiments were performed in the voltage range of 0.01-1.5 V considering $LiMnPO_4$ as the working electrode and WO_3 as both the reference and counter electrodes.

6.2.3 Results and Discussion

Figure 6.2.1a shows the XRD pattern of the synthesized $LiMnPO_4$ and all the diffraction peaks could be indexed to the orthorhombic crystal structure of $LiMnPO_4$ (JCPDS no. 74-0375) with a *Pnmb* space group. FESEM image of $LiMnPO_4$ indicates

formation of plate like structure with lateral dimension of approximately 200 nm-1 μm (Figure 6.2.1b). TEM image also further supports the 2D structure of $LiMnPO_4$ (Figure 6.2.1c) and crystallinity could be seen from HRTEM image (Figure 6.2.1d).

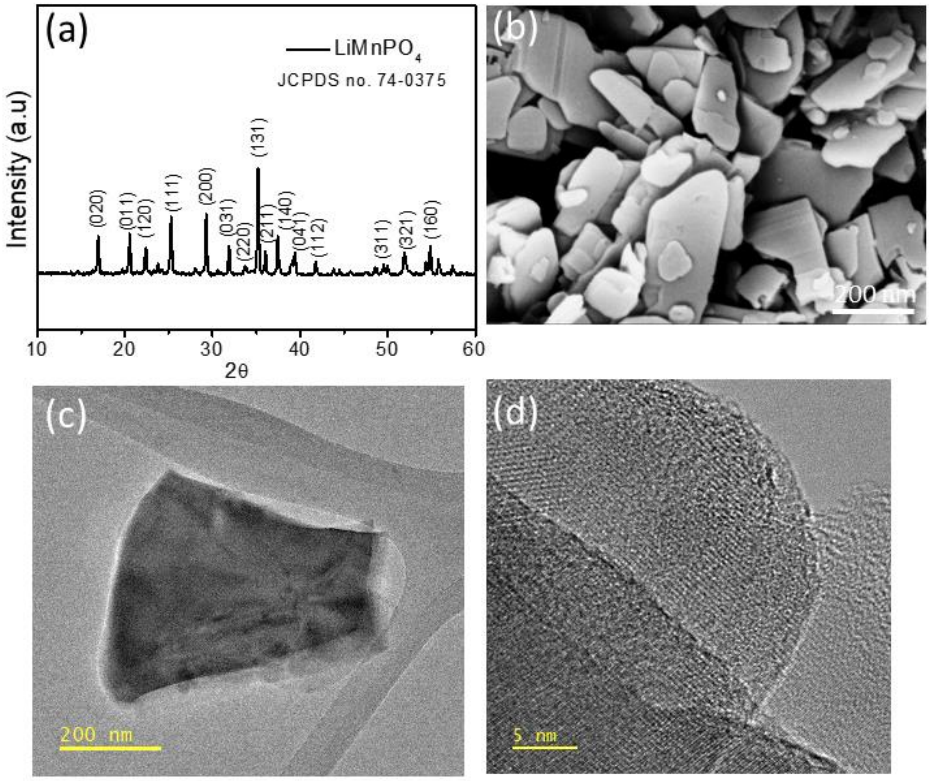

Figure 6.2.1 (a) XRD pattern, (b) FESEM image, (c) TEM and (d) HRTEM images of $LiMnPO_4$.

Figure 6.2.2a shows the CV profiles of $LiMnPO_4$ in 1 M $AlCl_3$ aqueous electrolyte at a scan rate of 2.5 mVs^{-1}. It could be clearly observed that there are two sharp cathodic peaks (labeled as A and B) at 0.85 V and 1.04 V. The peak B is stronger than peak A. However, only one anodic peak (C) is identified at 1.10 V. This phenomenon is in contrast to the electrochemical behavior of $LiMnPO_4$ in 1 M LiCl aqueous electrolyte. As shown in Figure 6.2.2b, in this case, the CV profiles exhibit broad cathodic and anodic peaks around 0.88 V and 0.61 V. CV experiment of $LiMnPO_4$ in 1 M $AlCl_3$ aqueous electrolyte at different scan rates are shown in Figure 6.2.3 and the linear dependence between peak current response and square root of scan rate indicates a diffusion-controlled Al^{3+} ion intercalation and deintercalation process in $LiMnPO_4$ [7].

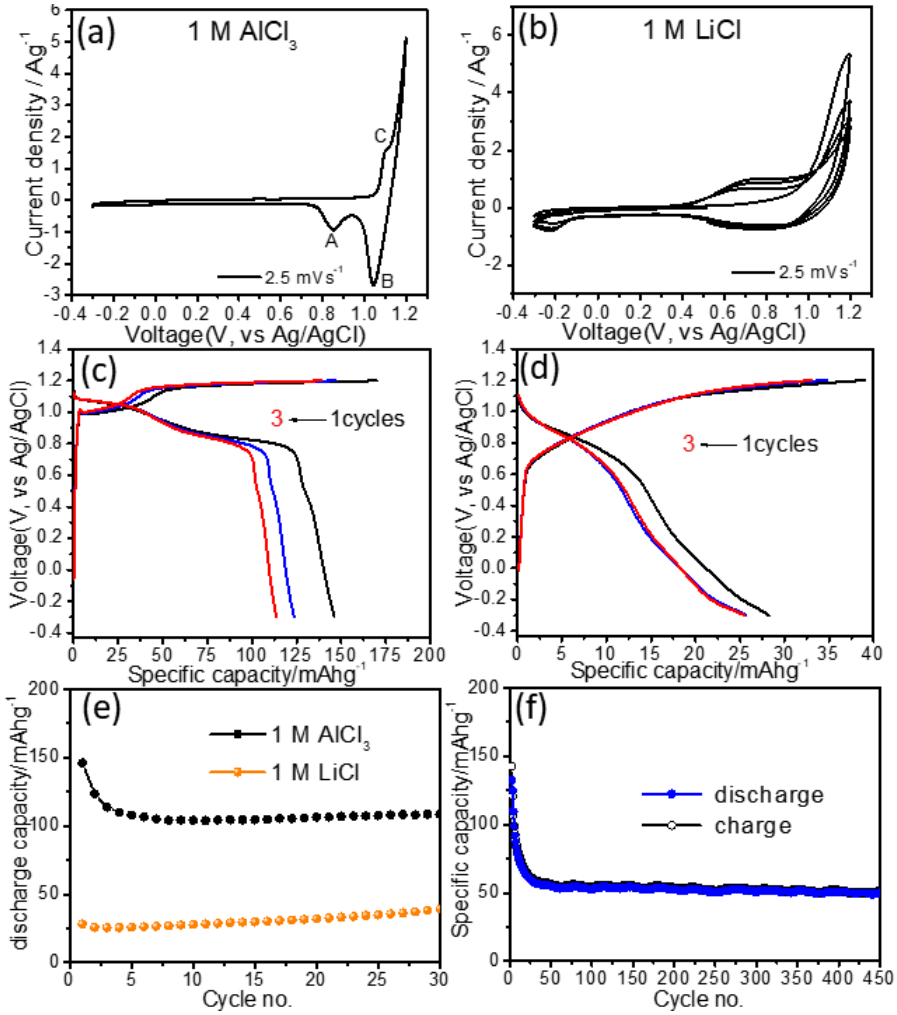

Figure 6.2.2 CV profiles of $LiMnPO_4$ in (a) 1 M $AlCl_3$ and (b) 1 M LiCl aqueous electrolytes. Galvanostatic discharge/charge profiles in (a) 1 M $AlCl_3$ and (d) 1 M LiCl aqueous electrolytes, variation of discharge capacities with cycle number at current density of (e) 1 Ag^{-1} and (f) 2.5 Ag^{-1}.

The CV outcome was further corroborated with galvanostatic discharge/charge measurements. Figure 6.2.2c shows the discharge/charge profiles of $LiMnPO_4$ in 1 M $AlCl_3$ aqueous electrolyte a current density of 1 Ag^{-1}. There are two discharge plateaus at 1.09 V and 0.86 V which are consistent with the CV measurement. An initial discharge capacity of 146 $mAhg^{-1}$ is estimated. On the other hand, the discharge/charge profiles of $LiMnPO_4$ in 1 M LiCl aqueous electrolyte show a kink at around 0.8 V rather than a flat discharge plateau in the discharge cycles (Figure 6.2.2d). Moreover, $LiMnPO_4$ shows an initial discharge capacity of only 28 $mAhg^{-1}$ in this case. The variation of discharge capacities with cycle number clearly indicates that electrochemical performance of $LiMnPO_4$ is much better in case of Al^{3+} ion (Figure 6.2.2e).

In addition, $LiMnPO_4$ exhibits stable specific capacity of 50 $mAhg^{-1}$ over 450 cycles at a current rate of 2.5 mAg^{-1} (Figure 6.2.2f), which was not supported in case of LiCl electrolyte.

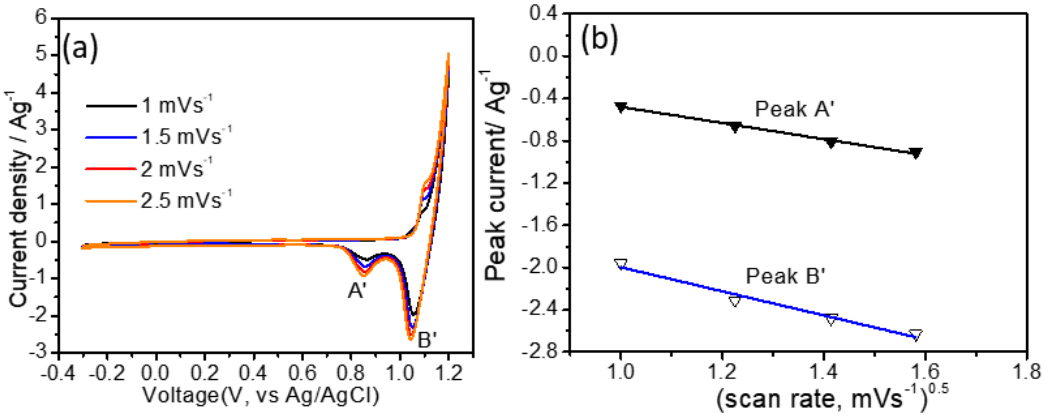

Figure 6.2.3 CV profiles of $LiMnPO_4$ at different scan rates in 1 M $AlCl_3$ aqueous electrolyte, and (b) linear dependence between peak current response and square root of scan rate according to the equation $I=k\gamma^{0.5}$ (where k is a constant). The peaks (A/ and B/) marked by the arrows are considered here.

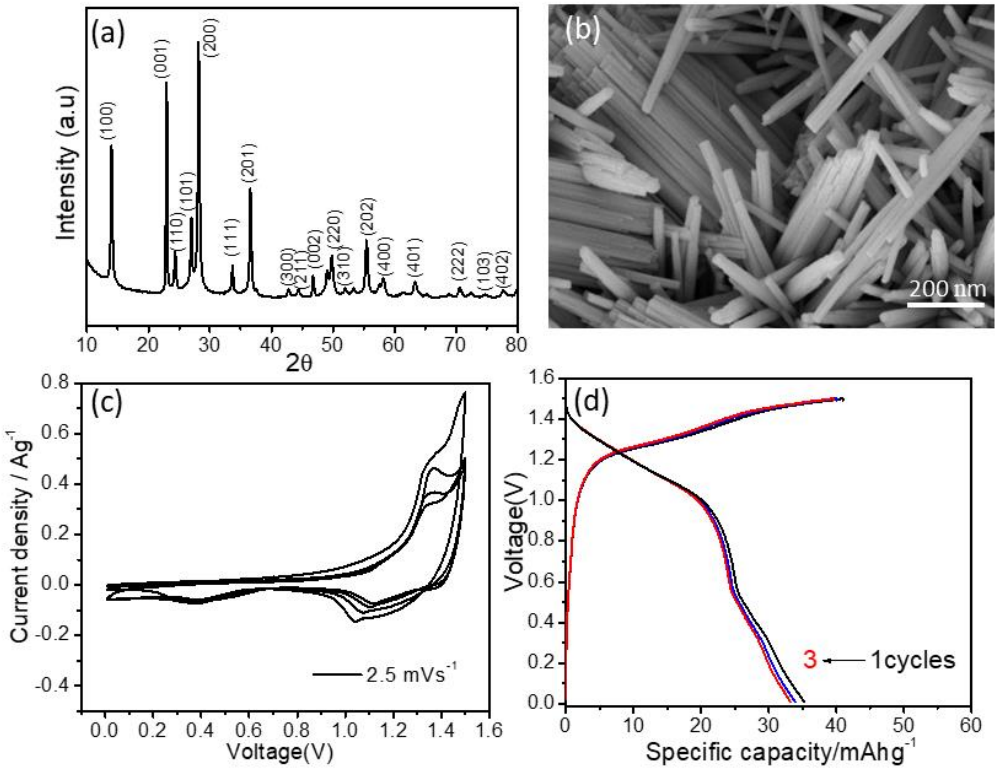

Figure 6.2.4 (a) XRD pattern and (b) FESEM image of WO_3, for $LiMnPO_4$//WO_3 cell (a) CV profile at a scan rate of 2.5 mVs^{-1} and (d) galvanostatic discharge/charge profiles in 1 M $AlCl_3$ electrolyte at current of 0.5 Ag^{-1}.

With this information at disposal, a rechargeable Al^{3+} ion cell was assembled using $LiMnPO_4$ as cathode and WO_3 as anode in 1 M $AlCl_3$ aqueous electrolyte. It is noted here that our group previously examined the feasibility of Al^{3+} ion storage in WO_3 electrode and found that redox activities could be seen at negative potential i.e., after -0.4 V (vs Ag/AgCl) [6]. Hence, WO_3 is selected as anode. WO_3 nanorod was synthesized as per the previous report [8]. The XRD pattern and FESEM image of the synthesized WO_3 are shown in Figure 6.2.4a, b. Figure 6.2.4c shows the CV profile of the assembled $LiMnPO_4//WO_3$ cell at a scan rate of 2.5 mVs^{-1}. A very broad cathodic peak in the range of 1-1.4 V and a minor peak at 0.38 V could be seen, whereas only one anodic peak appears at around 1.3 V could be observed. This is again reflected in the discharge/charge profiles. There is one discharge plateau extending over the potential range 1-1.4 V and a charge plateau in the potential range of 1.2-1.4 V (Figure 6.2.4d). The $LiMnPO_4//WO_3$ cell shows very stable cycling behavior. The estimated discharge capacity is in the range of 27-30 $mAhg^{-1}$ over 200 cycles at current rate of 0.5 Ag^{-1} (Figure 6.2.5).

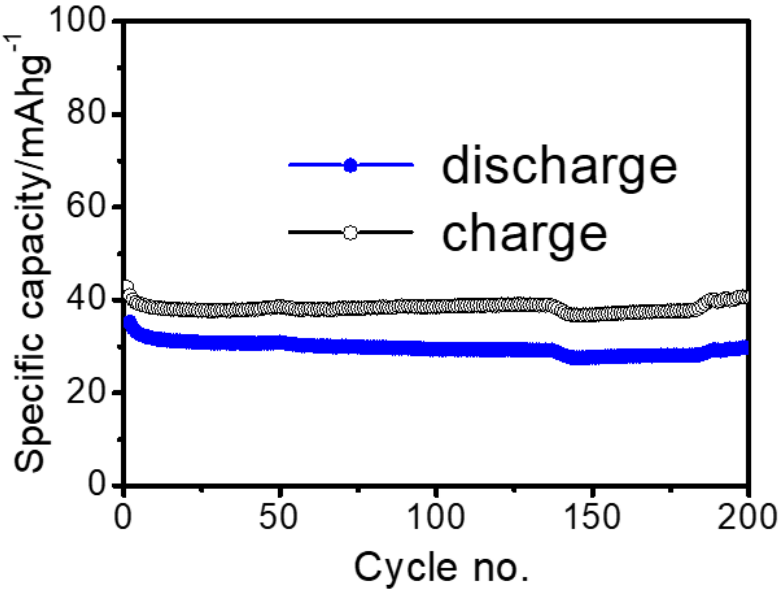

Figure 6.2.5 Variation of specific capacities with cycle number in 1 M $AlCl_3$ aqueous electrolyte at a current rate of 0.5 Ag^{-1}.

6.2.4 Conclusion

In summary, the ability of $LiMnPO_4$ to electrochemically store Al^{3+} ion in aqueous electrolyte is demonstrated in this chapter. It is found that $LiMnPO_4$ could deliver discharge capacity as high as 146 $mAhg^{-1}$ at a current rate of 1 Ag^{-1}. Based on it, a fully rechargeable Al^{3+} ion cell is demonstrated with $LiMnPO_4$ as cathode and WO_3 as anode. This cell exhibits excellent cycling stability over 200 cycles with a discharge capacity of 27-30 $mAhg^{-1}$ at a current rate of 0.5 Ag^{-1}.

6.2.5 References

[1] Vanchiappan, A., Joe, G., Sung, L. Y. and Srinivasan, M. $LiMnPO_4$ – A next generation cathode material for lithium-ion batteries *J. Mater. Chem. A.*, 1: 3518-3539, 2013.

[2] Fan, J., Yu, Y., Wang, Y., Wu, Q.-H., Zheng, M., and Dong, Q. Nonaqueous synthesis of nano-sized $LiMnPO_4$@C as a cathode material for high performance lithium-ion batteries. *Electrochim. Acta,* 194: 52-58, 2016.

[3] Gong, Z., and Yang, Y. Recent advances in the research of polyanion-type cathode materials for Li-ion batteries. *Energy Environ. Sci*. 4: 3223-3242, 2011.

[4] Ragupathi, V., Panigrahi, P., and Nagarajan, G. S. Enhanced electrochemical performance of nanopyramid-like $LiMnPO_4$/C cathode for lithium–ion batteries. *Appl. Surf. Sci.,* 495: 143541, 2019.

[5] Pan, X.-L., Xu, C.-Y., Hong, D., Fang, H.-T., and Zhen, L. Hydrothermal synthesis of well-dispersed $LiMnPO_4$ plates for lithium-ion batteries cathode. *Electrochim. Acta,* 87: 303– 308, 2013.

[6] Lahan, H., and Das, S.K. Reversible Al^{3+} ion insertion into tungsten trioxide (WO_3) for aqueous aluminum-ion batteries. *Dalt. Trans.* 48: 6337-6340, 2019.

[7] Wang, J., Polleux, J., Lim, J., and Dunn, B. Pseudocapacitive contributions to electrochemical energy storage in TiO_2 (anatase) nanoparticles. *J. Phys. Chem. C*, 111:14925-14931, 2007.

[8] Wang, J., Khoo, E., Lee, P.S., and Ma, J. Synthesis, assembly, and electrochromic properties of uniform crystalline WO_3 nanorods. *J. Phys. Chem. C* 112: 14306, 2008.